Lab on a Chip

Cite this: *Lab Chip*, 2012, **12**, 4683–4692

www.rsc.org/loc

PAPER

Blood compatible microfluidic system for pharmacokinetic studies in small animals†

Laurence Convert,[ac] Frédérique Girard Baril,[a] Vincent Boisselle,[a] Jean-François Pratte,[b] Réjean Fontaine,[b] Roger Lecomte,[c] Paul G. Charette[a] and Vincent Aimez*[a]

Received 14th May 2012, Accepted 22nd August 2012
DOI: 10.1039/c2lc40550d

New radiotracer developments for nuclear medicine imaging require the analysis of blood as a function of time in small animal models. A microfluidic device was developed to monitor the radioactivity concentration in the blood of rats and mice in real time. The microfluidic technology enables a large capture solid angle and a reduction in the separation distance between the sample and detector, thus increasing the detection efficiency. This in turn allows a reduction of the required detection volume without compromising sensitivity, an important advantage with rodent models having a small total blood volume (a few ml). A robust fabrication process was developed to manufacture the microchannels on top of unpackaged *p-i-n* photodiodes without altering detector performance. The microchannels were fabricated with KMPR, an epoxy-based photoresist similar to SU-8 but with improved resistance to stress-induced fissuring. Surface passivation of the KMPR enables non-diluted whole blood to flow through the channel for up to 20 min at low speed without clotting. The microfluidic device was embedded in a portable blood counter with dedicated electronics, pumping unit and computer control software for utilisation next to a small animal nuclear imaging scanner. Experimental measurements confirmed model predictions and showed a 4- to 19-fold improvement in detection efficiency over existing catheter-based devices, enabling a commensurate reduction in sampled blood volume. A linear dose-response relationship was demonstrated for radioactivity concentrations typical of experiments with rodents. The system was successfully used to measure the blood input function of rats in real time after radiotracer injection.

Introduction

Positron emission tomography (PET) and single photon emission computed tomography (SPECT) are currently the leading clinical imaging tools in nuclear medicine.[1,2] These imaging modalities are widely used for diagnostic and follow-up studies in oncology and cardiology. They involve the intravascular administration of a radiolabeled molecule, the radiotracer, followed by static or dynamic acquisition of images of the radiotracer biodistribution to scrutinize metabolic or physiologic disorders. New radiotracers are continuously being developed to improve diagnostic accuracy and reliability. Before being used in humans, new radiolabeled molecules have to be fully characterized in small animal models through pharmacokinetic studies.[3]

In addition to imaging, such studies require dynamic blood analysis during the imaging sequence involving repetitive blood sampling, commonly drawn manually, followed by blood plasma separation and radiochemical analysis of each sample to isolate the radiotracer from its metabolites.[4,5] However, repetitive manual blood sampling and analysis is technically difficult, time-consuming and hard to perform without affecting the animal homeostasis, especially with mice (~1.4 ml total blood volume).

Automated devices can be used to facilitate blood micro sampling,[6] however, samples have to be separated and measured off-line in a well counter, which can be limiting for short half-life radioisotopes like ^{15}O (2 min), ^{13}N (10 min) or even ^{11}C (20 min). Whole blood radioactivity concentration as a function of time, the so-called *input function*, can be monitored on a region of interest (ROI) in PET images[7,8] or using online blood counters.[9–11] However, the plasma and metabolite fractions cannot be estimated from such measurements. No integrated devices have yet been proposed to provide a full characterization of new radiotracers in small animals including plasma separation, radioactivity monitoring and chemical separation of metabolites.

[a]*Nanofabrication and Nanocharacterization Research Center, Department of Electrical and Computer Engineering, Université de Sherbrooke, 2500 Bd Université, Sherbrooke, QC, J1K 2R1, Canada. E-mail: Vincent.Aimez@USherbrooke.ca; Fax: +1(819)821-7937; Tel: +1(819)821-8000 #62137*
[b]*Sherbrooke Medical Devices Research Group, Department of Electrical and Computer Engineering, Université de Sherbrooke, 2500 Bd Université, Sherbrooke, QC, J1K 2R1, Canada*
[c]*Sherbrooke Molecular Imaging Centre, Department of Nuclear Medicine and Radiobiology, Université de Sherbrooke, 3001 12th Ave. North, Sherbrooke, QC, J1H 5N4, Canada*
† Electronic Supplementary Information (ESI) available. See DOI: 10.1039/c2lc40550d

With their range of demonstrated functionalities, reduced analysis time, cost, reagent quantities and human manipulations,[12,13] microfluidic technologies are a very attractive solution to provide full characterisation of new radiotracers in rodent nuclear imaging.

In this work, we present a key building block for such an integrated microfluidic chip: a real time microfluidic blood radiation monitoring chip (Fig. 1). After an overview of the theoretical background and prior art for radiation detection within microfluidic chips, the proposed design is described and the microfluidic detector fabrication process is detailed. The microfluidic chip was embedded in a blood counting system and characterised for sensitivity to common PET and SPECT radiotracers. A dose response curve was obtained from an aqueous radioactive solution. Finally, the system was employed to measure an input function in a rat using ^{18}F-FDG.

Theoretical background

In typical nuclear imaging experiments with small animals, radiotracer blood concentration rapidly increases during the bolus injection of a radiotracer, typically within a few seconds. Within a few minutes after the injection, the tracer penetrates into the tissues, rapidly lowering the blood concentration, until equilibrium in the exchanges between the blood and tissues is reached. The radiotracer blood concentration then stabilises to, typically, a few tens of radioactive disintegrations per second (Becquerel, Bq) per µl. In the mouse model, only a few hundred µl at most are available for real time analysis over a 10–30 min period. As a consequence, the detection volume must be kept at a minimum, around 1 µl at any given time during measurement.

To faithfully reproduce the input function, the detector must then integrate a small signal over a very short time period, roughly 1 s, on a very small detection volume, around 1 µl. To obtain a statistically significant signal, the detection efficiency must therefore be very high. For typical radiation detection experiments, the detection efficiency relies on three parameters: (1) the detector intrinsic efficiency (2) the capture solid angle and (3) the attenuation of the emitted radiation in the interface layer between the sample and the detector sensitive volume. The capture solid angle is maximized by minimizing the distance between the source and the detector and by having a source the same size or smaller than the detector. The attenuation of the radiation depends on the type of radiation to be detected.

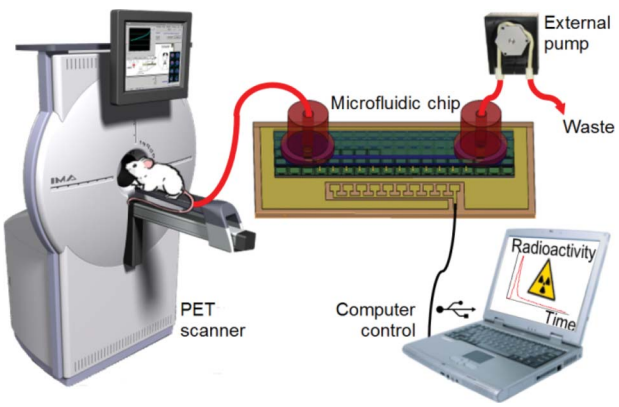

Fig. 1 Microfluidic blood counter connected to an animal for PET pharmacokinetic studies.

PET imaging is based on positron emitting radioisotopes. Positrons, the antiparticles of electrons also known as β^+, are emitted in a continuous energy spectrum peaking at around 1/3 of the maximum emission energy, $E_{\beta max}$. The maximum energy depends on the isotope and ranges from 0.6 to 1.7 MeV for common PET tracers (^{64}Cu, ^{18}F, ^{11}C, ^{13}N, ^{68}Ga and ^{15}O).[2] Positrons are typically stopped within a few millimetres in biological tissues, then they annihilate with an electron in the medium, producing two 511 keV annihilation photons that go through the body and are detected by the PET scanner. SPECT imaging relies on gamma (γ) radiation, typically between 60 keV and 250 keV, directly emitted by common radionuclides such as ^{99m}Tc, ^{67}Ga, ^{111}In, ^{123}I and ^{201}Tl.[2] The gamma emission is typically accompanied by Auger and conversion electrons. Another class of radionuclides used for metabolic radiotherapy decay mostly or solely by β^- particle emission.[14] Measuring the input function of these radiopharmaceuticals would also be useful to calculate the radioactivity exposure of the target and other organs.

Thus, for blood radioactivity monitoring, it is possible to detect either the photon (annihilation or gamma) or the charged particle (β^+, β^- or electrons). High-energy photon detection requires a high-density crystal, generally between 1 and 2 cm thick, which is not appropriate for microsystem integration. Therefore, charged particle detection is preferred for miniaturized devices as it can be performed with silicon detectors of a few hundred micrometer thickness (the typical thickness of Si wafers).

Charged particles interact with matter by gradually transferring kinetic energy to substrate electrons along their path ranging from zero to a few millimetres, depending on the particle energy and medium composition. Even a very thin interface of a few hundred micrometers thick can stop the low-energy particles before they even reach the detector. To achieve the detection efficiency required for pharmacokinetic studies in small animals with PET and SPECT, this interface layer must thus be minimized.

Prior art

Detectors for optical applications have been integrated in microfluidic devices for about twenty years, mainly for fluorescence measurements.[15,16] However, the requirements for charged particle detection are quite different. In particular, most microfluidic devices with integrated fluorescence detection have an optically transparent channel floor with an optical filter between the sample and the detector. The resulting interface thickness (0.2 to 3 mm thick), however, would stop most of the charged particles emitted by PET and SPECT radioisotopes. In the few cases where the interface was very thin (below a few tens of micrometers),[17] the detectors were typically optimized for visible photon detection (shallow depletion region), which is not appropriate for radiation detection.

A radiation detector with high detection efficiency for charged particles was proposed by Burns *et al.*[18] for possible integration into a microfluidic system, but the authors opted for fluorescence detection in the actual integrated system[19] because of the higher

detection efficiency for their application. More recently, radiation detectors have been coupled to microfluidic devices for cell imaging[20,21] or radiolabeled protein adsorption in microchannel walls,[22,23] but the sensitivities remained limited due to absorption of low-energy β radiation in the microfluidic channel walls. Consequently, these devices were restricted to the detection of relatively energetic β^+ particles, and thus, to PET tracer detection. To overcome these limitations, the proposed design incorporates a polymer microfluidic channel directly above a radiation detector array, providing a large capture solid angle and eliminating all unnecessary interfaces between the blood and the detection layer. The detection efficiency is thereby increased, enabling a commensurate reduction in sampled blood volume at equal sensitivity—an important advantage in small animal models.

Fabrication of polymer microchannels on top of existing electronics has received growing interest in the past few years.[24] Among the available technologies, which include replica moulding and hot embossing, photopatternable polymers are often preferred due to their compatibility with current microelectronic industry standards. In particular, SU-8 (Microchem Corp., USA), an epoxy-based photoresist, is a popular choice because of its high chemical resistance, good optical and mechanical properties, as well as its ability to be processed over a wide range of thicknesses.[24] SU-8 microchannels have been integrated on top of electronics for CMOS compatible labs-on-a-chip.[25] However, internal stress generated during the patterning process tends to produce fissuring[26] which is problematic for microfluidic devices. Very precisely controlled temperature ramps are required during the resist soft and post-exposure bakes to minimize such stress, lengthening the overall processing time.

Microchem has recently introduced KMPR, an epoxy-based photoresist which is less subject to internal stress, leading to shorter processing time and superior resistance to fissuring.[27] To date, KMPR has mainly been used for electroplating moulds.[28,29] In previous work, we described the use of KMPR as a structural material for microfluidic devices[30] and prototype chips were investigated for charged particles detection.[31,32] We also proposed a method to render KMPR hemocompatible.[33] In this work, the fabrication process of an optimized device is detailed, including the microfluidics and contact to the underlying detection electronics. The device was embedded in a blood counting system including dedicated electronics, software and pumping unit.

Materials and methods

Detection principle and geometry

Charged particles transfer kinetic energy to substrate electrons creating free charges. In the depleted region of a reverse biased diode, these charges migrate rapidly to the electrodes and are collected, generating a photocurrent. With the depletion region extending through the whole wafer thickness, *p-i-n* photodiodes are well suited for charged particle detection.[34] Existing charged particle counters for measuring blood radioactivity[9,35–37] are typically made of a catheter from the animal cannula placed against a detector (Fig. 2A). Such systems involve a $\sim$700 μm thick interface between the blood sample and the detection area that stops low energy beta particles, thus reducing detection efficiency. The proposed microfluidic device is made of a flat rectangular KMPR microchannel fabricated over commercial unpackaged silicon *p-i-n* photodiodes (Fig. 2B).

This design has two advantages over catheter-based systems: the interface thickness is limited to the microchannel floor layer (a few μm) and the aspect ratio of the microchannel (width $\gg$ height) leads to a quasi 2D measuring geometry and, thus, to a large capture solid angle approaching 2π. The resulting increased detection efficiency enables a significant reduction in the detection volume without compromising sensitivity, making this approach better suited to the small blood volume of rodents. Though the junctions with a catheter at either end of the fluidic device and change in lumen shape (circular *vs.* rectangular) may lead to dead volumes and turbulence, these effects are expected to be negligible as explained below.

Furthermore, this technology is biocompatible and readily amenable to the integration of other microfluidic functionalities (plasma separation, microsampling, chemical species separation, *etc.*) required for full on-chip characterisation of new radiotracers in the context of small animal nuclear imaging.

Microfluidic chip fabrication process

The fabrication process was based on non-sacrificial photolithography over an SiO_2 passivated Si wafer, compatible with most hard substrates (Fig. 2B). This process provided straightforward fabrication with very precise microchannel positioning over an electronic device. A polymer-coated glass top was used to seal the channels and to provide access holes while allowing channel content visualization. The process provided a uniform polymer interface to the fluid inside the microchannel. The hydrodynamic and interface properties were then simple to model. Access holes geometry was designed to fit Nanoports (Upchurch, USA), allowing easy catheter connection.

Wall layer design. The channels were fabricated over 4 inch wafers containing a continuous matrix of 2×2 mm^2 *p-i-n* photodiodes (Excelitas Technologies, Vaudreuil-Dorion – formerly PerkinElmer Optoelectronics). The wafers were diced into individual strips that were processed independently. The fluid microchannels were designed to exactly overlap a row of twelve adjacent photodiodes to have sufficient detection volume for efficient pharmacokinetic studies with rodent models. The channels were U-shaped to keep the diode anodes close to the pattern edge while limiting the total footprint, to maximize the fabrication yield. The overall dimensions of the resulting pattern photomask were 34×8 mm^2. The fluid microchannels have a 37 μm $\times$ 1.1 mm cross section and a length of 31.5 mm (1.3 μl). Except for the Nanoport bonding zones, the unused filled areas of the wall layer were patterned in a grid shape (300 μm wide lines, 2.3 mm pitch) to limit internal stresses and reduce the bonding surface (Fig. S1A in the ESI†). The microchannel walls were made larger than the grid lines (500 μm wide) to ensure good sealing. Unlike in our previous designs,[31,32] metallic tracks were added to displace the anode contact away from the microchannel, simplifying wire bonding and optimizing the detection area (Fig. S1B in the ESI†). To minimize stray capacitance, the anode tracks were fabricated over the KMPR floor layer and kept as short as possible.

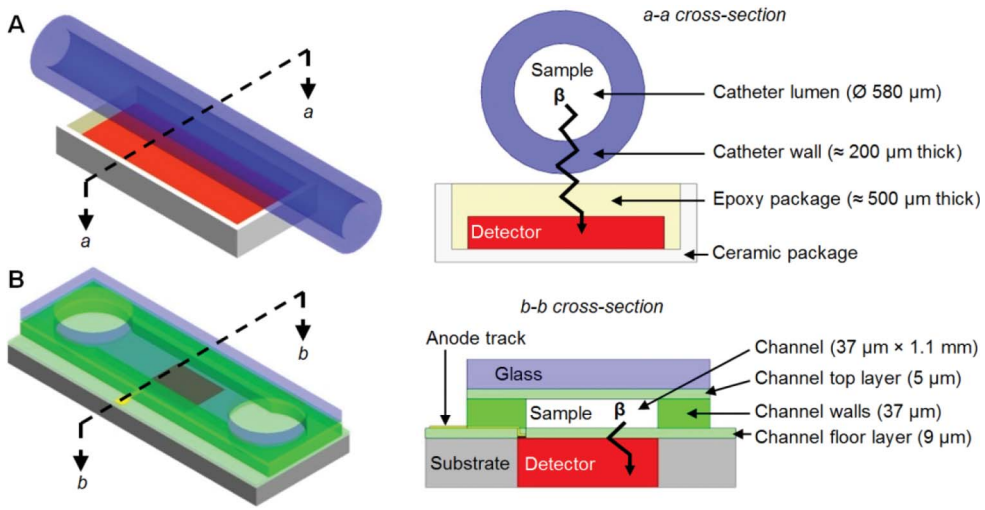

Fig. 2 Schematic views of a catheter-based blood counter (A) and of the microfluidic blood counter (B, only one diode shown) (not to scale).

General microfabrication parameters. Unless otherwise specified, the photolithographic parameters were as follows: Shipley S1813 spin coating at 2000 rpm, 2 min soft bake at 115 °C; AZ nLOF 2020 spin coating at 3000 rpm, 1 min soft bake at 110 °C, 5 s exposure, 1 min post exposure baked (PEB) at 110 °C, and 2 min development in Microchem MF319; Microchem KMPR1005 spin coating at 2000 rpm, edge bead removal with acetone, 5 min soft bake at 100 °C, 40 s exposure, 2 min PEB at 100 °C, 2 min development with Microchem SU-8 developer; KMPR1005 25% in SU-8 thinner spin coating at 2000 rpm, 1 min soft bake at 100 °C, 25 s exposure, 2 min PEB at 100 °C, 15 s development in MF319 : H_2O (1 : 1).

Before resist spinning, samples were dehydrated in a stove at 125 °C for 30 min. Both nLOF and KMPR were exposed with a broadband aligner through a high-pass i-line filter. Soft bake and PEB were performed on a hot plate while hard bake were performed in a stove. All photoresist developments were made by immersion. The samples were rinsed in DI-water for 2 min then dried with nitrogen after each wet cleaning, wet etch or development. Samples were rinsed in IPA for 20 s after SU-8 developer development before the DI-water rinse. Descum was performed in plasma O_2 at 50 W for 2 min (Plasmaline 211, Tegal Corporation). Resist stripping was performed with solvents in ultrasonic bath, 5 min in acetone followed by 5 min in IPA.

Sample preparation and passivation (Step A, B). The Excelitas wafers, passivated with a ~30 nm SiO_2–Si_3N_4 layer, were first protected with S1813 photoresist and diced in 42 × 16 mm^2 dies to add a 4 mm-wide area around the channel pattern for edge beads (Fig. 3A). After resist stripping, an additional 300 nm SiO_2 passivation layer was deposited on the dies using plasma enhanced chemical vapor deposition (PECVD, HFSiO, 300 °C). Contact regions over the anodes were defined by photolithography using nLOF 2020. After descum, the SiO_2 was dry etched in CF_4 (AOE ICP, Surface Technology Systems). The nLOF mask was then stripped and the KMPR1005 floor layer added (Fig. 3B). The dies were then hard baked for 3 h at 180 °C.

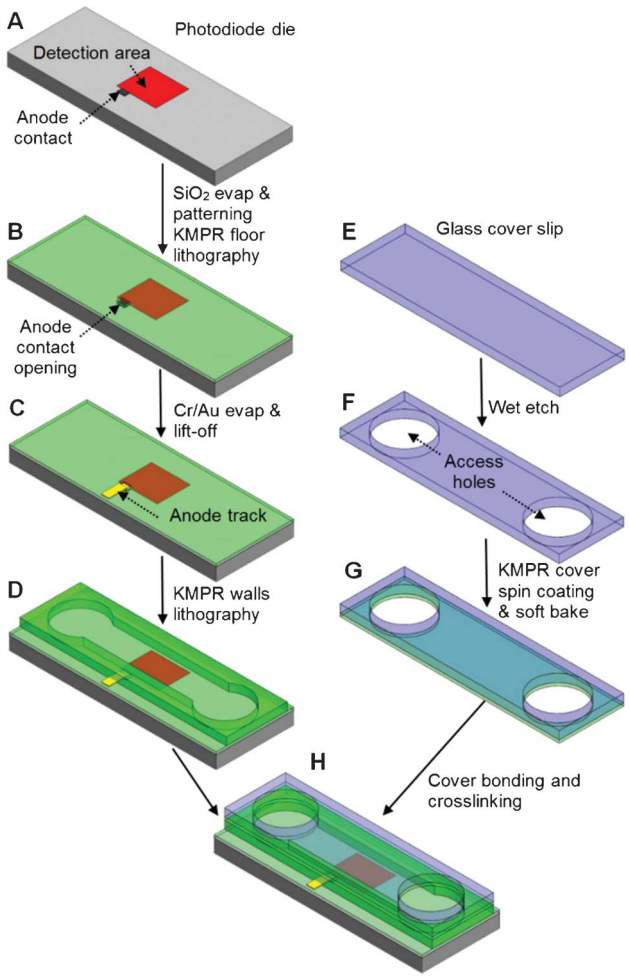

Fig. 3 Simplified fabrication process diagram for the KMPR microfluidic radiation detector (only one diode shown, not to scale).

Anode track lift-off (Step C). Anode track patterns were defined using nLOF 2020 (spin coating at 1500 rpm, 8 s exposure and development for 3 min 30 s). After descum, anode surfaces were cleaned in BOE for 5 s, rinsed in running DI-water for

5 min and dried with nitrogen just before metal evaporation. The metal films, 3 nm Cr and 300 nm Au, was then evaporated on the dies using an inclined rotating stage. Lift-off was performed in acetone for 1 h 30 min (Fig. 3C). A thin KMPR1005 25% floor layer was then deposited on the dies, patterned to allow wire bonding over the end of the gold tracks, and hard baked for 1 h at 180 °C.

Microchannel wall lithography (Step D). After dehydration, KMPR1025 was deposited on the dies and they were placed under vacuum for 10 min for degassing. The dies were then spun at 2000 rpm, edge beads were removed with acetone and the samples were left to rest for 5 min before soft bake (15 min at 100 °C) to increase layer uniformity. The layer was then exposed for 50 s and baked for 5 min at 100 °C. The development was performed in SU-8 developer for 8 min 30 s (Fig. 3D). Finally, the dies were hard baked for 1 h at 180 °C.

Cover etching (Step E, F). Borosilicate cover slips, 130 to 160 μm thick, were used as the channel covers (25 × 75 mm^2 #1 thickness, Bellco Glass Inc., Fig. 3E). The glass cover slips were wet etched to have the same surface area as the KMPR wall pattern with two access holes. The cover slips were first cleaned with soap (Alconox, Cole-Parmer Instrument Co) then immersed for 15 min in piranha solution (1 : 1). Chromium was sputtered on one side (300 nm) and patterned using KMPR 1005 as a mask. The cover slips were then hard-baked for 1 h at 180 °C. After descum, chromium was wet etched using Chrome Etch (CR7S10, OM Group Inc.) for 5 min and the cover slips were glued to Si wafers to protect the backside during glass etching (AZ P4903 spin coated at 3000 rpm, cover slip application, bake for 30 min at 125 °C in an oven). Access holes were etched using a BOE : HCl (2 : 1) solution[38] at 40 °C for 1 h 30. P4903 was then stripped with solvents (10 min), KMPR was removed with piranha (1 : 1, 15 min) and chromium was stripped with Chrome Etch (Fig. 3F).

Cover bonding (Step G, H). The cover slips were bonded using KMPR in a process similar to the one usually employed with SU-8.[39] After dehydration, KMPR1005 was spin coated at 6000 rpm and soft-baked for 10 s at 100 °C (Fig. 3G). The cover slips were then applied over the channel walls and the alignment was adjusted under an optical microscope.

The assembly was then baked on a hot plate at 100 °C for 1 min, exposed for 30 s then baked under pressure ($\approx 1.10^6$ Pa) for 5 min at 100 °C then for 1 h at 180 °C (Fig. 3H).

Microfluidic chip packaging. The chips were diced to position the gold pads close to the die edge, thus reducing the length of the wire bonding. To prevent residue from obstructing the microchannels, access holes were protected with semi-tack during dicing. The contact surfaces were cleaned with IPA. The Nanoport adhesive ring and then the Nanoport itself were placed over the access holes and maintained in place using the supplier's clamps. The assembly was then baked for 1 h at 180 °C.

After microchannel fabrication, the devices were glued to the metal plane of a gold-plated custom-made PCB using conductive epoxy (H20E, Epoxy Technology Inc.), ensuring that the back contact was connected to the common cathode. Eight anode (top) contacts were then wire-bonded to a common PCB pad to electrically connect the photodiodes in parallel.

Hemocompatibility surface treatment. Passivation of the microfluidic chip itself was performed by flowing BSA solution (10 mg ml^{-1} in phosphate buffer saline) through the system at 2 μl min^{-1} for 2 h. An accepted blocking agent for plasma proteins with many polymeric material surfaces,[40] BSA passivation has recently been shown to also be effective with KMPR.[33]

Device characterisation

Device electrical and functional performances were evaluated. As a reference, all measurements were repeated with an existing catheter-based geometry[9] consisting of a packaged *p-i-n* photodiode (S3588-08, 3 × 30 mm^2, Hamamatsu Corporation) with a catheter (0.58 mm ID, 0.965 mm OD, Intramedic PE50, Becton Dickinson) centered on its surface (Fig. 2A).

Electrical characterisation. CV–IV measurements were made on each diode with a SMU (4200-SCS, Keithley) before microfabrication processing, after the floor layer lithography and after the cover bonding to monitor any changes in photodiode performance. Electrical characteristics were also measured after wire bonding.

Modeled detection efficiency. Theoretical detection efficiency was evaluated, for both the microfluidic chip and existing catheter-based geometries, in terms of energy loss at the interface layer (Table 2) between the blood sample and the detection area, as well as the geometrical detection efficiency.

When a charged particle goes through a layer of thickness X_i (cm), the energy loss, E (MeV), is estimated using the equation:[41]

$$E = \int_{X_i}^{0} S(x)\rho dx \quad (1)$$

where S (MeV cm^2 g^{-1}) is the particle collision stopping power (the average rate of energy loss per unit path length due to Coulomb interactions), ρ (g cm^{-3}) is the medium density, and x (cm) is the thickness of the medium. The energy loss must be integrated over the thickness (1 μm integration step) because the particle gradually loses energy and S is a function of the particle energy. Tabulated values[42] of S as a function of the particle energy and atomic composition of the three types of absorbing media were used in eqn (1) for (1) catheter walls (Polyethylene, C_2H_4, ρ = 0.94 g cm^{-3}, mean excitation energy = 45.7 eV), (2) KMPR microchannel floor layer (epoxy, $C_{22}H_4O_{25}$, ρ = 1.2 g cm^{-3}, mean excitation energy = 91.7 eV) and (3) epoxy package (same values as KMPR). Energy loss was computed for two incident energies (E_i) of 190 keV and 836 keV, corresponding to the mean β energy[43] of a low and a high energy PET isotope, ^{64}Cu and ^{68}Ga, respectively.

Numerical solid angle simulations were performed with the TracePro software (Lambda Research, Littleton, MA) to determine the geometrical detection efficiency (number of particles inside the microchannel incident onto the detector as a fraction of the total number of emitted particles), η_{geo} (%), for

both the microfluidic chip design described here and the catheter-based detection geometry.

Functional characterisation. Experimental confirmation of the model predictions was undertaken by embedding the microfluidic chip and the catheter-based detector in the same blood counting system. This system consists of two separate hardware modules (Fig. S2 in the ESI†) and control software. The detector unit includes the detector chip connected to a custom made signal processing board for pulse shaping and amplification. The control unit includes the control electronics for radiation pulse counting, USB communication with a personal computer and pump speed control for the miniature peristaltic pump (P625/900.133, Instech Laboratories Inc.). A graphical user interface is used to set-up experiment parameters, display the blood time-activity curve in real time and process recorded data.

For direct charged particle detectors, the sensitivity is dependent on the incident particle energy and must be characterized for each tracer. The microfluidic chip and the Hamamatsu detector (with PE50 catheter) were injected with 10 kBq μl^{-1} solutions of two of the most common PET radioisotopes (^{18}F, ^{11}C) and a 30 kBq μl^{-1} solution of the most common SPECT isotope (^{99m}Tc). The average count rate, m (cps), acquired during two minutes was corrected for radioactive decay and used to calculate the device absolute detection efficiency, η (%):

$$\eta = \frac{m}{C \times V} \quad (2)$$

where C (Bq μl^{-1}) is the calibrated solution concentration and V (µl) is the device detection volume. An ''improvement factor'' (see Table 3), defined as the detection efficiency of the microfluidic design presented here relative to the detection efficiency of catheter-based systems, η_{device}/n_{conv}, was computed.

The system linearity was characterised by measuring the decay of a static ^{11}C source injected in the microchannel. For dynamic linearity assessment, a dose-response curve was then determined by injecting a solution of ^{18}F-FDG, 27 MBq in 5.1 ml of water, followed by four successive 1 : 2 manual dilutions at 5 min intervals. The withdrawing pump was set to 30 µl min^{-1}, typical of experiments with rats. The microfluidic chip was then flushed with non-radioactive water to ensure that no residual radioactivity remained in the microchannel.

Finally, a 334 g Sprague-Dawley rat was anaesthetized with isoflurane (2.5% + 1.5 l min^{-1} O_2) and cannulated in the caudal artery with a 5-cm-long PE50 catheter preloaded with heparinized saline (0.9%, 50 U ml^{-1}). A 40-cm-long PE10 catheter (0.28 mm ID, 0.61 mm OD, Intramedic PE10, Becton Dickinson) was connected to the PE50 catheter and to the microfluidic chip. PE50 was chosen for cannulation to best fit the animal artery and PE10 was chosen for blood transport to reduce the dead volume between the animal and the detector. PE10 catheter was also used to connect the output of the microfluidic chip to the pump tubing (silicon tubing, 0.020′′ ID, 8 cm long, P625/TS020S, Instech Laboratories Inc.) and the pump to the waste. The microfluidic blood counter and all tubing were flushed with heparinized saline before connecting the animal to the PE10 catheter. The pump was then started at 30 µl min^{-1} and the rat was injected with 35 MBq of ^{18}F-FDG (caudal vein, 0.3 ml at 0.9 ml min^{-1}). The pump was stopped 20 min after injection, the cannula removed from the animal and the system flushed with heparinized saline. Animal experiments were performed in accordance with the guidelines of the in-house Ethics Committee for Animal Experiments and the Canadian Council on Animal Care.

Results and discussion

Microfluidic chip fabrication process

Sample preparation and passivation. The 300 nm SiO_2 layer below the KMPR floor layer was a precautionary measure that ensured uniformly good electrical isolation of the underlying photodetector electronics in case of any fluid leakage due to micro-defects of the polymer film. The photoresist nLOF was chosen as the masking layer for contact opening in SiO_2, rather than the KMPR floor layer, to avoid the increased roughness resulting from SiO_2 dry etching. As both nLOF and KMPR are negative photoresists, the same photomask could be used for contact opening in SiO_2 and KMPR floor. Note that a KMPR hard bake was necessary to ensure sufficient chemical resistance during lift-off.

Anode track lift-off. The lift-off was facilitated by using AZ nLOF 2020 resin spin-coated at 1500 rpm leading to a 3.1 µm thick layer with retrograde profiles. BOE cleaning before evaporation was required because developers and plasma O_2 descum oxidize the anode. The inclined rotating stage led to good step coverage even for the 300 nm thick metal layer over the 9 µm KMPR step (Fig. 4A).

Gold was chosen because it provided a better electrical contact to the underlying anode than pure aluminum. Further optimization would be required to obtain a good electrical contact with a CMOS compatible metal. Typical lift-off in Remover at 70 °C (Microchem Corp.) was not possible without strongly affecting the KMPR layer, even after hard bake. However, hard-baked KMPR, like SU-8, has good resistance to acetone supporting the lift-off process. In a small number of cases, stress-induced fissures needed to be filled with KMPR1005 25% film after lift-off. This thin 350 nm film was developed with diluted MF319 because SU-8 developer or pure MF319 were too aggressive.

Microchannel wall lithography. KMPR lithography with EBR yielded 37 µm-wide channel sidewalls with a vertical profile similar to SU-8 (Fig. 4B). The fabrication process is however more straightforward as no complex temperature ramps are needed to avoid excess stress and cracks in the resist. The reduced stress also increased surface adherence over Si and SiO_2.

Cover etching. As the glass cover slips were less than 200 µm thick, special care was taken to limit tensile stress induced by the chromium mask layer. The metal was deposited by sputtering rather than evaporation. The wet etch performed with BOE:HCl solution[38] led to an etch rate slightly above 2 µm min^{-1} (HCl eliminates the BOE/glass reaction products, increasing the etch rate). Even if wet etching with a hard mask requires several processing steps, it was preferred to laser micromachining because it produces a V-shape hole profile that reduces edge beads around the holes during the KMPR cover layer spinning.

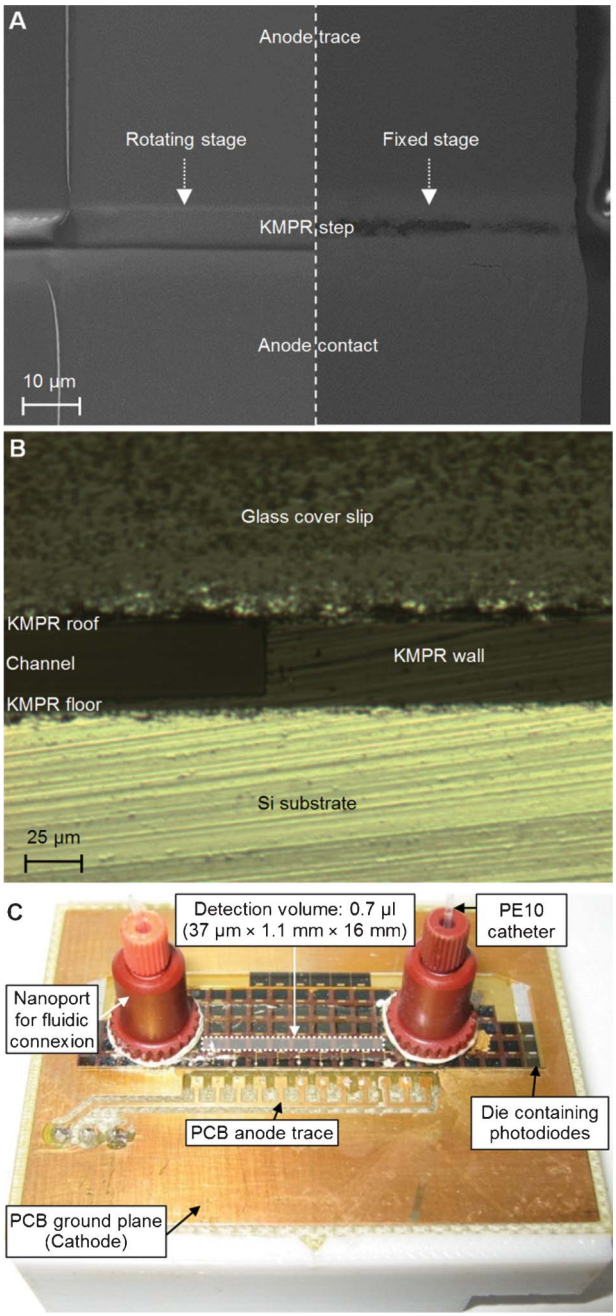

Fig. 4 A. Electron microscope view of the step coverage after evaporation with a rotating stage compared to a fixed stage (top view with 45° slope of the microscope stage). B. Cross sectional view of a 35 µm deep microchannel wall on a Si substrate. The cross section was obtained by dicing the chip after cover bonding (optical microscope, 10X). C. Photograph of the final chip after wire bonding.

Cover bonding. A cross sectional view of a complete device after bonding is shown in Fig. 4B. The cover layer was 5 µm thick and the channel walls remained vertical after bonding. Devices were tested up to 15×10^5 Pa ($\approx$10 ml min^{-1}) fluid pressures without failure. KMPR is therefore an effective adhesive layer for microfluidic channel sealing. Wall layer flatness is of great importance for successful bonding. For channel thickness below 20 µm, those parameters are even more critical to avoid channel obstruction. Thinner adhesive layers (KMPR1005 dilution) were tested for such thin channels. Although cover bonding was facilitated, the overall adhesive strength was reduced.

Microfluidic chip packaging. A photograph of the final chip after wire bonding is shown in Fig. 4C on a Teflon support. A gold-plated pin header on the back side is used for connection to the signal processing PCB. Nanoports allow connection from PE10 catheters (cannula from the animal artery) to the microchannel with minimal dead volume and adhesive contamination of the fluid path.

Despite laminar flow in both the catheter with the circular section and the microchannel with the flat rectangular section, the geometrical change may introduce some turbulence and add a small smoothing of fast radioactive concentration change, contributing to the total dispersion of the system. This effect is however considered to be negligible compared to the dispersion occurring inside the catheter itself.

Device characterisation

Electrical characterisation. The mean capacitance and dark current at −30 V bias for single diodes before microfabrication processing, after SiO_2/KMPR passivation, and at the end of the complete process, are presented in Table 1. An example of capacitance and dark current as a function of reverse voltage is presented in Fig. S3 in the ESI† for a single diode.

Passivation did not affect the capacitance and the gold track has a small impact. Dark current was slightly reduced after passivation and remained unchanged with the anode track and wall layer. The bonded device electrical performances (eight diodes in parallel, total 19.2 mm^2 detection surface) are comparable to the reference Hamamatsu detector (90 mm^2 detection surface) used in the catheter-based geometry (Table 1).

Though the microfluidic channel was designed for twelve diodes along the fluid path, eight diodes were functional on any single device on average, due to gold track fabrication defects. The resulting physical characteristics of the tested devices are presented in Table 2. Gold track fabrication yield could be improved by increasing the chromium adhesion layer thickness from 3 to 10 nm and by optimizing the KMPR floor layer lithography to obtain slightly positive sidewall angles, increasing the step coverage. A larger number of working diodes would increase the device sensitivity, as the measured radioactivity would rise linearly with the detection volume while the electronic noise rises as the square root of the number of diodes, leading to a commensurate improvement in minimum detectable radioactivity concentration.

Modeled detection efficiency. Theoretical energy loss calculations (Table 2) show that low energy particles will be entirely absorbed within the interface layers above the detector in the catheter-based geometry, whereas almost no particles should be lost to absorption in the microfluidic device described here. The proposed device is therefore expected to be highly beneficial for low β energy PET isotope detection. Furthermore, 120 keV conversion electrons emitted by ^{99m}Tc do not reach the active detection area in the catheter-based geometry, rendering the

Table 1 Electrical properties of tested devices (measured for bias = −30 V). The final microfluidic device consists of 8 diodes bonded in parallel on a PCB

Parameters	Capacitance (pF)		Dark current (nA)	
	Microfluidic	Catheter-based	Microfluidic	Catheter-based
Single diode before processing	2.56 ± 0.05	—	0.48 ± 0.04	—
Single diode with floor layer	2.61 ± 0.01	—	0.36 ± 0.03	—
Single diode with track & microchannel	3.77 ± 0.03	—	0.37 ± 0.05	—
Final device	32.0[a]	52.8	2.0[a]	2.1

[a] 8 diodes.

most widespread SPECT radioisotope undetectable, unlike with our device.

Solid angle calculations (Table 2) predict a quasi-optimal geometrical detection efficiency of the microfluidic chip (considering that half of the particles are emitted in the direction opposite to the detector). The geometrical detection efficiency is 1.25× better than our previous prototypes[32] and 1.66× better than the catheter-based geometry.

Functional characterisation. Measured detection efficiencies for both the proposed microfluidic design and catheter-based geometries confirm the theoretical calculation (Table 3). As expected, the increase in detection efficiency is more significant for low-energy particles. The model calculations predict that the catheter-based geometry cannot detect conversion electrons emitted by ^{99m}Tc. The detected event rate (∼500 cps) above background (set to a ∼5 cps threshold before each experiment) is therefore attributable to the 140 keV gamma radiation of ^{99m}Tc, which has a very low but non-zero probability of interaction in a 300 μm thick Si detector (0.06% photoelectric and 1% total). The resulting measured detection efficiency (0.2%) is however insufficient for any typical animal model experiment. The relatively low detection efficiency of ^{99m}Tc compared to ^{18}F or ^{11}C (4% compared to 39% and 47%) in our microfluidic chip is due to the reduced emission probability of the detected particle (9% compared to ∼100%). Even though further improvements in detection efficiency would be required for experiments with rats, the typical blood radioactivity in mice is high enough to warrant studies with ^{99m}Tc.

Note that the summed error on count rate (∼5 cps) and solution concentration (∼20 kBq for a 400 μl solution) remained around 1% for all tracers for both the microfluidic and the catheter-based detector, leading to an error on the improvement factor of less than 1%. As both the microfluidic and the catheter-based detector have the same response to 140 keV photons, the improvement factor will not be affected by counts due to a contribution from 140 keV gamma rays interaction.

Thus, the microfluidic detector has high detection efficiency for PET tracers and is able to detect SPECT tracers. This high detection efficiency allows the reduction of the detection volume by a factor corresponding to the improvement factor in detection sensitivity, while keeping the same counting statistics. For instance, the detection volume can be decreased from 7.9 μl to 900 nl for ^{18}F radiotracers, a considerable improvement for use with small animal models where limited blood volume is an issue.

For up to 10 kcps, the response deviation from linearity is less than 1%. This count rate is obtained for concentrations of 32 kBq μl^{-1} with ^{11}C that are well above that typically encountered in small animal experiments. The dose response curve of Fig. 5A shows five plateaus with an exponential decrease in mean plateau height for successive 1 : 2 dilutions (Fig. S4 in the ESI†). The injected radioactive concentrations are representative of typical concentrations used in rats and mice studies, showing the system linearity under flow-through conditions. Furthermore, the count rate variations in each plateau agrees well with the Poisson statistics inherent to radioactive emission processes (Fig. S4B in the ESI†): the standard deviation of the count rate closely follows the square root of the count rate.

This experiment also demonstrates that the radioactive molecules do not adsorb to the KMPR walls as the count rate goes back to the background rate (set to a few cps before the radioactive injection) when the fluidic input is switched back to non-radioactive water. This behaviour was confirmed with whole blood by switching the microfluidic blood counter input back to non-radioactive saline solution after experiments. Finally, these results illustrate that fast changes in radioactive concentration are smoothed due to radiotracer dispersion inside the catheter. Such effects are typical of online counters and can be corrected with numerical modelling by fitting the input function time constant for a known injection speed.[44]

The whole-blood input function measured from the caudal artery of a rat is presented in Fig. 5B. Blood radioactivity rapidly rises after the radiotracer intravenous injection, followed by a bi-exponential decrease as the tracer penetrates into the tissues.

Table 2 Physical characteristics of tested devices (PE = polyethylene, Ep = epoxy, E_i = incident energy)

Parameters	Microfluidic	Catheter-based
Interface thickness (μm)	9 (Ep)	700 (200 PE + 500 Ep)
Detection volume (μl)	0.7	7.9
Energy loss (keV) for E_i = 190 keV	3	190
Energy loss (keV) for E_i = 836 keV	2	142
Geometrical detection efficiency (%)	49.3	30

Table 3 Absolute detection efficiency, η, for microfluidic device and catheter-based detector measured for different isotopes (10 kBq μl^{-1} for ^{11}C and ^{18}F, 30 kBq μl^{-1} for ^{99m}Tc)

Isotope	Particle energy (keV)	Emission probability (%)	Microfluidic η (%)	Catheter-based η (%)	Improvement factor
^{11}C	0–961	100	46.9	12.1	3.9
^{18}F	0–634	97	38.8	4.4	8.8
^{99m}Tc	120	9	3.8	0.2	19

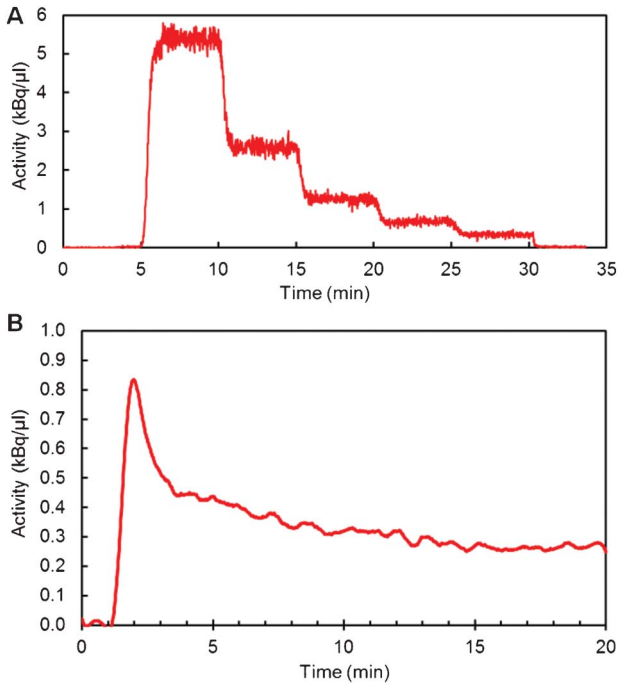

Fig. 5 A. Dose-response curve for a 5.2 kBq μl^{-1} ^{18}F-FDG solution, after four successive 1 : 2 dilutions and switching back to non-radioactive water. This curve was corrected for detector efficiency, propagation delay and radioactive decay. No corrections were required for the background count rate. B. Input function measured from a rat injected with 35 MBq of ^{18}F-FDG. The curve was corrected for detector efficiency, radioactive decay and averaged to reduce statistical noise (Savitzky-Golay method, 100 points).

This typical curve shape obtained from the whole blood of a rat shows that the microfluidic blood counter is suitable for small animal experiments. It also demonstrates that passivated KMPR is highly hemocompatible as non-diluted rat whole blood flowed through the thin channels (37 µm thick) at low speed for 20 min without clotting. The device was tested with whole blood at 10 µl min^{-1} for the same duration without any deleterious effect, indicating that the microfluidic blood counter would also be suitable for studies with a mouse model.

Conclusions

KMPR microchannels were fabricated directly atop unpackaged *p-i-n* photodiodes to reduce the distance between the radioactive fluid sample and the detector in a microfluidic blood radioactivity counter. KMPR is easy to process, robust and does not adversely affect photodiode performance. The device geometry and electronics provide high detection efficiency for β radiation and conversion electron detection in small blood volumes compatible with pharmacokinetic PET and SPECT studies with rodent models. The response is linear with the radioactive concentration and the microfluidic blood counter was successfully used to measure rat whole blood radioactivity after injection of a PET tracer.

Future work will validate the microfluidic blood counter in pharmacokinetic studies with small animals and evaluate the robustness of the BSA passivation for reuse. Further developments will focus on the addition of plasma separation and microsampling functionalities on-chip to provide full characterization of new radiotracers.

Acknowledgements

The authors would like to thank Dr Henri Dautet of Excelitas Technologies for supplying the *p-i-n* photodiode wafers, Véronique Dumulon-Perreault and Mélanie Archambault from the Sherbrooke Molecular Imaging Centre for the support with animal experiments and the staff of the Université de Sherbrooke Nanofabrication and Nanocharacterisation Research Center (CRN^2) for microfabrication support. This work was supported by the Canadian Institutes of Health Research (CIHR) grant #MOP-86717 and NanoQuébec. The Étienne-Le Bel Clinical Research Centre hosting the Sherbrooke Molecular Imaging Centre is a FRQ-S funded research organization.

References

1 D. Bonekamp, D. A. Hammoud and M. G. Pomper, *Appl. Radiol.*, 2010, **39**, 10–21.
2 S. R. Cherry, J. A. Sorenson and M. E. Phelps, *Physics in Nuclear Medicine*; 3rd edn; Saunders, pp. 544: Philadelphia, 2003.
3 G. C. Kagadis, G. Loudos, K. Katsanos, S. G. Langer and G. C. Nikiforidis, *Med. Phys.*, 2010, **37**, 6421–6442.
4 P. Dupont and J. Warwick, *Methods*, 2009, **48**, 98–103.
5 K. Serdons, A. Verbruggen and G. M. Bormans, *Methods*, 2009, **48**, 104–111.
6 H.-M. Wu, G. Sui, C.-C. Lee, M. L. Prins, W. Ladno, H.-D. Lin, A. S. Yu, M. E. Phelps and S.-C. Huang, *J. Nucl. Med.*, 2007, **48**, 837–845.
7 M. Bentourkia and H. Zaidi, *PET Clin.*, 2007, **2**, 267–277.
8 J. Kim, P. Herrero, T. Sharp, R. Laforest, D. J. Rowland, Y.-C. Tai, J. S. Lewis and M. J. Welch, *J. Nucl. Med.*, 2006, **47**, 330–336.
9 L. Convert, G. Morin-Brassard, J. Cadorette, M. Archambault, M. Bentourkia and R. Lecomte, *J. Nucl. Med.*, 2007, **48**, 1197–1206.
10 J. Breuer, R. Grazioso, N. Zhang, M. Schmand and K. Wienhard, *Phys. Med. Biol.*, 2010, **55**, 5883–5893.
11 S. Yamamoto, M. Imaizumi, E. Shimosegawa, Y. Kanai, Y. Sakamoto, K. Minato, K. Shimizu, M. Senda and J. Hatazawa, *Phys. Med. Biol.*, 2010, **55**, 3813–3826.
12 L. Kang, B. G. Chung, R. Langer and A. Khademhosseini, *Drug Discov. Today*, 2008, **13**, 1–13.
13 G. M. Whitesides, *Nature*, 2006, **442**, 368–373.
14 C. J. Anderson and J. S. Lewis, *Expert Opin. Ther. Pat.*, 2000, **10**, 1057–1069.
15 H. Gai, Y. Li and E. S. Yeung, *Top. Curr. Chem.*, 2011, **304**, 171–201.
16 B. Kuswandi, D. Nuriman, J. Huskens and W. Verboom, *Anal. Chim. Acta*, 2007, **601**, 141–155.
17 V. Namasivayam, R. Lin, B. Johnson, S. Brahmasandra, Z. Razzacki, D. T. Burke and M. A. Burns, *J. Micromech. Microeng.*, 2004, **14**, 81–90.
18 M. A. Burns, C. H. Mastrangelo, T. S. Sammarco, F. P. Man, J. R. Webster, B. N. Johnsons, B. Foerster, D. Jones, Y. Fields, A. R. Kaiser and D. T. Burke, *Proc. Natl. Acad. Sci. U. S. A.*, 1996, **93**, 5556–5561.
19 M. A. Burns, B. N. Johnson, S. N. Brahmasandra, K. Handique, J. R. Webster, M. Krishnan, T. S. Sammarco, P. M. Man, D. Jones, D. Heldsinger, C. H. Mastrangelo and D. T. Burke, *Science*, 1998, **282**, 484–487.
20 J. S. Cho, N. T. Vu, Y. H. Chung, Z. T. F. Yu, R. W. Silverman, R. Taschereau, H.-R. Tseng and A. F. Chatziioannou, *IEEE Nucl. Sci. Symp. Conf. Rec.*, 2006, **4**, 1977–1981.
21 N. T. Vu, Z. T. F. Yu, B. Comin-Anduix, J. N. Søndergaard, R. W. Silverman, C. Y. N. Chang, A. Ribas, H.-R. Tseng and A. F. Chatziioannou, *J. Nucl. Med.*, 2011, **52**, 815–821.
22 M. Lavén, S. Wallenborg, I. Velikyan, S. Bergström, M. Djodjic, J. Ljung, O. Berglund, N. Edenwall, K. E. Markides and B. Långström, *Anal. Chem.*, 2004, **76**, 7102–7108.

23 J. S. Cho, R. Taschereau, S. Olma, K. Liu, Y.-C. Chen, C. K.-F. Shen, R. M. Van Dam and A. F. Chatziioannou, *Phys. Med. Biol.*, 2009, **54**, 6757–6771.
24 T. Pan and W. Wang, *Ann. Biomed. Eng.*, 2011, **39**, 600–620.
25 Z.-C. Peng, Z.-G. Ling, M. Tondra, C.-G. Liu, M. Zhang, K. Lian, J. Goettert and J. Hormes, *J. Microelectromech. Syst.*, 2006, **15**, 708–716.
26 D. W. Johnson, A. Jeffries, D. W. Minsek and R. J. Hurditch, *J. Photopolym. Sci. Technol.*, 2001, **14**, 689–694.
27 K.-S. Ou, H.-Y. Yan and K.-S. Chen, *Strain*, 2008, **44**, 267–271.
28 C. H. Lee and K. Jiang, *J. Micromech. Microeng.*, 2008, **18**(055032), 7pp.
29 Y.-M. Shin, D. Gamzina, L. R. Barnett, F. Yaghmaie, A. Baig and N. C. Luhmann, *J. Microelectromech. Syst.*, 2010, **19**, 683–689.
30 L. Convert, V. Aimez, P. Charette and R. Lecomte, *1st Microsyst. Nanoelec. Res. Conf. Rec.*, 2008, 105–108.
31 L. Convert, F. Girard Baril, V. Boisselle, J.-F. Pratte, R. Fontaine, V. Aimez, P. Charette and R. Lecomte, *IEEE Nucl. Sci. Symp. Conf. Rec.*, 2010, 2128–2131.
32 L. Convert, F. Girard Baril, A. Renaudin, É. Grondin, A. Jaouad, V. Aimez, P. Charette and R. Lecomte, *Nucl. Instrum. Methods Phys. Res., Sect. A*, 2011, **652**, 735–738.
33 L. Convert, V. Chabot, P.-J. Zermatten, R. Hamel, J.-P. Cloarec, R. Lecomte, V. Aimez and P. G. Charette, *Sensors and Actuators B. Chemical*, 2012, DOI: 10.1016/j.snb.2012.07.061.
34 G. F. Knoll, *Radiation Detection and Measurement*; 3rd edn; John Wiley and Sons, pp. 816: New York, 2000.
35 L. Eriksson, S. Holte, C. Bohm, M. Kesselberg and B. Hovander, *IEEE Trans. Nucl. Sci.*, 1988, **35**, 703–707.
36 S. Ashworth, A. Ranicar, P. M. Bloomfield, T. Jones, A. A. Lammertsma, *In Quantification of Brain Function using PET*; Academic Press: San Diego, 1996, pp. 62–66.
37 S. Yamamoto, K. Tarutani, M. Suga, K. Minato, H. Watabe and H. Iida, *IEEE Trans. Nucl. Sci.*, 2001, **48**, 1408–1411.
38 R. Mazurczyk, G. El Khoury, V. Dugas, B. Hannes, E. Laurenceau, M. Cabrera, S. Krawczyk, E. Souteyrand, J.-P. Cloarec and Y. Chevolot, *Sens. Actuators, B*, 2008, **128**, 552–559.
39 J. Carlier, K. Chuda, S. Arscott, V. Thomy, B. Verbeke, X. Coqueret, J.-C. Camart, C. Druon and P. Tabourier, *J. Micromech. Microeng.*, 2006, **16**, 2211–2219.
40 K. R. Kamath and K. Park, *J. Appl. Biomater.*, 1994, **5**, 163–173.
41 D. W. Anderson, *Absorption of Ionizing Radiation*; University Park Pr, pp. 428: Baltimore, 1984.
42 National Institut of Standards and Technology http://physics.nist.gov/PhysRefData/Star/Text/ESTAR.html, last accessed 2012-04-10.
43 Berkeley Laboratory Isotopes Project http://ie.lbl.gov/education/isotopes.htm, last accessed 2012-02-15.
44 E. Meyer, *J. Nucl. Med.*, 1989, **30**, 1069–1078.